RESEARCH ARTICLE | JULY 01 2025

The effect of ICRH and NBI on tungsten transport in neon edge radiation cooled discharges in TEXTOR

J. Rapp ; S. Brezinsek ; G. D. Dhamale ; H. R. Koslowski ; A. Krämer-Flecken ; J. Ongena ; G. Sergienko

Phys. Plasmas 32, 072502 (2025)
https://doi.org/10.1063/5.0273526
CHORUS

The effect of ICRH and NBI on tungsten transport in neon edge radiation cooled discharges in TEXTOR

Cite as: Phys. Plasmas **32**, 072502 (2025); doi: 10.1063/5.0273526
Submitted: 31 March 2025 · Accepted: 16 June 2025 ·
Published Online: 1 July 2025

J. Rapp,[1] S. Brezinsek,[2] G. D. Dhamale,[1,a)] H. R. Koslowski,[2] A. Krämer-Flecken,[2] J. Ongena,[3] and G. Sergienko[2]

AFFILIATIONS

[1]Fusion Energy Division, Oak Ridge National Laboratory , Oak Ridge, Tennessee 37831, USA
[2]Institute of Fusion Energy & Nuclear Waste Management—Plasma Physics, Forschungszentrum Jülich, Jülich, Germany
[3]Laboratoire de Physique des Plasmas/Laboratorium voor Plasmafysica, ERM/KMS, EURATOM Association, Brussels, Belgium

[a)]Author to whom correspondence should be addressed: dhamalegd@ornl.gov

ABSTRACT

Tungsten is planned to be the plasma-facing material for the main chamber and divertor in future devices like ITER, SPARC, and DTT. To address risks associated with tungsten, R&D is being carried out on various toroidal confinement devices. One particular research question is related to the optimum heating mix for ITER. To investigate the influence of the heating scheme on the release and transport of tungsten, a comparison of neutral beam injection (NBI) and ion cyclotron resonance frequency (ICRF) heating was carried out in TEXTOR tungsten test limiter experiments. The experiments were performed under standard L-mode conditions and in radiative improved-mode operation with neon seeding and boronized walls covering the graphite plasma-facing components. The plasma was heated with hydrogen or deuterium NBI alone or with deuterium NBI in combination with H-minority, ion cyclotron resonance heating. A movable solid tungsten limiter was inserted through a limiter lock system into the edge plasma. The impurity release from this limiter was evaluated from visible spectroscopy. The tungsten concentrations in the plasma core were determined by extreme ultraviolet spectroscopy and bolometry. With deuterium NBI alone, strong central radiation and accumulation of W was observed. This can, however, be avoided by adding ICRF heating.

I. INTRODUCTION

While there were a few tokamaks operating with metal walls since a while (e.g., Alcator C-mod[1] and FTU[2]), in particular, the last 15 years have seen a change from graphite toward metallic walls in many tokamaks around the world. In particular, JET's change from carbon fiber composite (CFC) to an ITER-like wall made of beryllium tiles in the main chamber and a tungsten divertor has brought great insight on the erosion and impurity migration for ITER. The overall impurity migration picture is similar, with the main erosion source still being the main chamber wall and the transport of the erosion products to the apron of the inner divertor with a net W erosion source at the strike line when operating like ITER in vertical target configuration. In JET, the overall main chamber erosion with Be was strongly reduced compared to the graphite main chamber wall due to the absence of chemical erosion at low-impact energies.[3]

With a W first wall, the overall main chamber erosion will be reduced by orders of magnitude as seen in ASDEX Upgrade when turning from graphite to tungsten[4] and in initial predictive plasma–wall interaction modeling for ITER comparing the Be/W mix with full-W setup as discussed now.[5]

W is chemically inert, and hence, chemical erosion is absent. Physical erosion will dominate the erosion processes. Energetic charge exchange (CX) neutrals can contribute to the overall W-source as they overcome the sputtering threshold for D and T. Impurities, either intrinsic or extrinsic deliberately seeded impurities, dominate physical erosion process. The tungsten transport was found to be neoclassical in the plasma core, when sawteeth are absent[7] a long time ago and most recently also during the sawtooth cycle.[8] In the plasma edge, the radial convection is still believed to be neoclassical, but the radial anomalous diffusion is much higher than in the plasma core.

The neoclassical convection is determined by the ion temperature and ion density gradients. Both of these can be influenced by the heating scheme employed. In this contribution, a comparison of ion cyclotron resonance frequency (ICRF) and neutral beam injection (NBI)-heated discharges is done to elucidate their effects on the tungsten transport. Please note that generally ICRF heating can also have an effect on the tungsten source on plasma-facing components (PFCs) on the antenna Faraday screens or nearby PFCs. In the experiments reported here, all PFCs around the ion cyclotron resonance heating (ICRH) system were graphite and boronized. The advantage of the investigation here is addressing the impact of ICRH and NBI on the transport of W, independent of the tungsten source. Many of the high-Z tokamaks (i.e., ASDEX Upgrade,[9] C-mod,[10] and WEST[11]) do have a convolution of the ICRF-driven high-Z sources with the effect of ICRF on the impurity transport. ICRF-driven tungsten sources here mean enhanced localized tungsten sources due to rectified RF-sheath effects in the near-field at the antenna and the far-field on field lines connecting the RF-sheath with other plasma-facing components. In TEXTOR, the tungsten test limiter and the ICRF antenna are not magnetically connected. Hence, the experiments reported here aimed at deconvoluting the effect of ICRF-driven sources and high-Z impurity transport in ICRH plasmas. It should be mentioned that similar experiments were carried on the EAST tokamak.[12,13]

TEXTOR was a limiter tokamak with circular cross section operating mostly in L mode and with seeding impurities in the so-called radiative improved (RI) mode.[14,15] A general comparison of NBI and ICRF-heated discharges in TEXTOR can be found in Ref. 16.

The RI mode is a high-confinement regime with reduced ion temperature gradient (ITG)-driven turbulence.[17,18] While the effect of the edge transport (H-mode pedestal) on tungsten transport cannot be studied in TEXTOR, tungsten core transport can be investigated. The high-Z transport in the plasma core is thought to be mainly neoclassical in nature.[7,19] Anomalous transport channels due to ITG-driven turbulence or trapped electron modes (TEM) turbulence are thought to have less effect on the tungsten transport in the plasmas investigated here. However, they influence the transport of H and D and thus determine the profiles of the background ions. Dedicated experiments where the global energy confinement was kept constant by feedback control on the applied ICRF power should help to disentangle large variations in the global energy confinement on the impurity transport vs effects related to the background profile (gradient) effects on the neoclassical transport are presented in Sec. IV.

Furthermore, the information gained here is also relevant to the current ramp-up phase in limiter configuration for ITER. The edge electron densities and temperatures are similar in TEXTOR in comparison with ITER during this ramp-up phase. Simulations with SOLPS-ITER, DINA, and JINTRAC for ITER limiter plasma startup on tungsten show T_e at the last closed-flux surface (LCFS) in the range of 40 to 120 eV for n_e at the LCFS in the range of $1–12 \times 10^{12}\,\mathrm{cm}^{-3}$.[20]

For $n_{e,LCFS}$ of $6 \times 10^{12}\,\mathrm{cm}^{-3}$, the electron temperature at the LCFS is about 50 eV.[20] This is very similar to the conditions in TEXTOR as will be shown later. Also, the power into the scrape-off layer and the radiative power fraction in TEXTOR ($P_{SOL} = 0.6–1.1$ MW, $\gamma_{rad} = 0.5–0.9$) are in the range of ITER parameters.[20]

II. EXPERIMENTAL SETUP

A movable solid W-test limiter (Fig. 1) was inserted through a limiter lock into the edge plasma of TEXTOR ($R_0 = 175$ cm, $a = 46$ cm

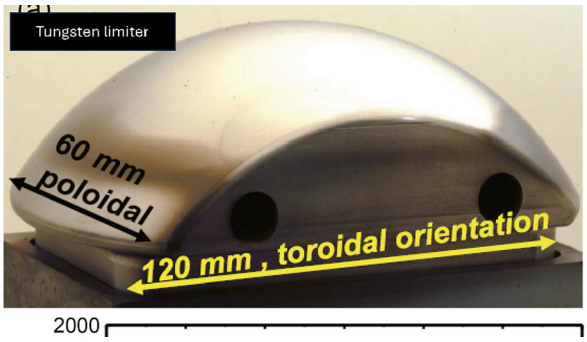

FIG. 1. Tungsten test limiter.[6] Reprinted with permission from Rubel *et al.*, Matter Radiat. Extremes **2**, 87–104 (2017). Copyright 2017 Authors, licensed under a Creative Commons Attribution (CC BY) license.

determined by the toroidal belt limiter ALT-II). Figure 2 shows the test limiter setup in TEXTOR with diagnostic access. The impurity release from this limiter was evaluated from visible spectroscopy at the limiter surface by measuring WI at 400.8 nm as well as using a CCD camera observing the limiter and using a 1.5 nm bandwidth filter to get spatial distributions of the tungsten source. In order to obtain tungsten neutral fluxes, the S/XB values (ratio of ionization to excitation rate) from the literature were used.[22] The W-flux presented here relates to the peak value of the spatial WI-light distribution on the spherical limiter surface (see also Fig. 1).

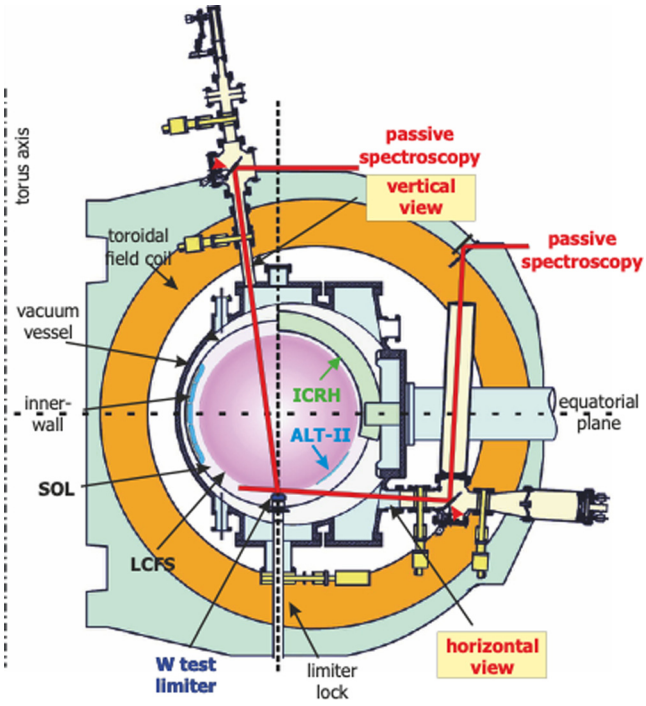

FIG. 2. Cross section of TEXTOR with test limiter setup and diagnostic access. Modified with permission from Rubel *et al.*, Matter Radiat. Extremes **2**, 87–104 (2017). Copyright 2017 Authors, licensed under a Creative Commons Attribution (CC BY) license.

The electron temperature and density at the plasma edge were determined by a helium beam diagnostic.[23] T_e at the edge of TEXTOR ($r = 46$ cm) was typically in the range of 50–80 eV. In this temperature range, the S/XB values are typically around 55. n_e at the edge of TEXTOR ($r = 46$ cm) is about 0.6×10^{13} cm^{-3}. For these T_e and n_e values and a magnetic field of 2.25 T, a prompt redeposition of tungsten[24] of about 90% in divertor geometry is expected. However, for the TEXTOR test limiter geometry, about 72% to 85% has been calculated with PIC simulations, while ERO simulations predict 55% redeposition.[25–27] Deuterium, carbon, and oxygen fluxes on the limiter were determined as well. A detailed analysis can be found in Ref. 28.

The impurities in the core plasma were obtained with extreme ultraviolet (XUV) spectroscopy and a 34-channel bolometric system. The concentration of tungsten was determined from the total radiation, assuming corona equilibrium and using the data of Post *et al.*[29] The local radiation in the plasma center was obtained from bolometry after inversion with tomographic techniques.[7] Since the intrinsic impurities in TEXTOR are carbon and oxygen, they do not contribute to the total radiation in the plasma center significantly.

Nevertheless, the background radiation (mainly from Bremsstrahlung of C and O) was subtracted from the total radiation with tungsten accumulation in the plasma core before determining the tungsten concentration. The XUV spectrometer is a grazing incidence spectrometer and measures the W-quasicontinuum (W^{30+}) in the spectral range of 4.5–7.0 nm. A typical XUV spectrum in TEXTOR is shown in Fig. 3. For our analysis, the W-quasicontinuum was integrated from 4.5 to 7.0 nm. However, a closer look to the spectrum reveals that the W-quasicontinuum is blended by boron lines.[30] The presence of boron lines is due to the fact that TEXTOR is boronized regularly. To eliminate the effect of boron lines and continuum radiation, tungsten concentrations were obtained from pairs of discharges (with the test limiter inserted or withdrawn).

The cross-calibration of the XUV spectrometer to the local radiation data from bolometry was done with the use of the data from Post *et al.*[29] in discharges where the radiation from tungsten in the center of the plasma was strong. Those were discharges with a high W-source by inserting the W-test limiter far into the plasma boundary and operating at higher boundary electron temperatures in low-density L modes. The XUV data were then used in discharges with lower W concentrations, where bolometry would not give reliable tomographic reconstructions for the evaluation of tungsten core densities. Here, it is assumed that the tungsten concentration profiles are flat, $n_z(r) \propto n_e(r)$. Deviations from this flat profile assumptions, due to accumulation of tungsten in the center for example, will lead to errors in the determination of the tungsten core concentration. In order to estimate the error, several variations of the radial profile were studied with the help of the MIST code.[31]

The radial profile of the W^{30+} ions (see Fig. 4) for flat tungsten concentration profiles and peaked tungsten concentration profiles has been calculated for a low-density case ($n_e = 2 \times 10^{13}$ cm^{-3}, $T_e = 1.7$ keV) and a high-density case ($n_e = 5 \times 10^{13}$ cm^{-3}, $T_e = 0.9$ keV). The T_e and n_e profiles for those MIST simulations are shown in Fig. 5.

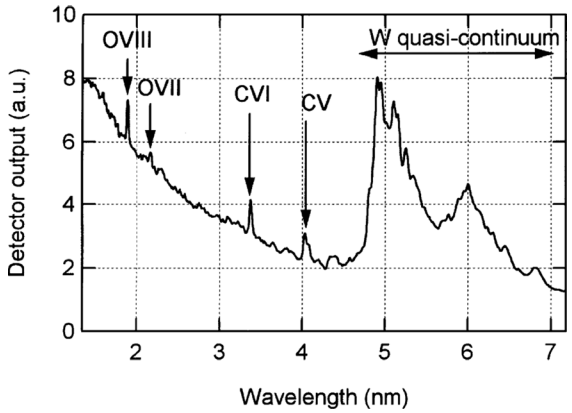

FIG. 3. A typical XUV spectrum obtained by the grazing incidence spectrometer in TEXTOR.[21] Reprinted with permission from Wada *et al.*, J. Nucl. Mater. **290**, 768–772 (2001). Copyright 2001 Elsevier.

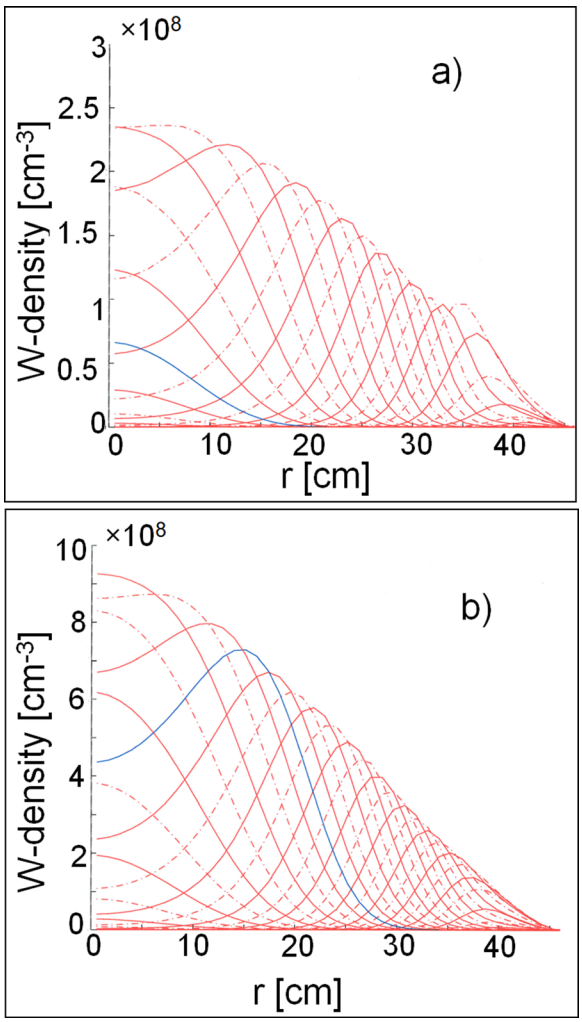

FIG. 4. MIST simulations for tungsten ion density distributions across the radius of TEXTOR. The blue line is for W^{30+} ions. W-density profiles for flat W concentration profiles and constant radiation power: (a) line-averaged $n_e = 5 \times 10^{13}$ cm^{-3}, $T_e = 0.9$ keV; (b) line-averaged $n_e = 2 \times 10^{13}$ cm^{-3}, $T_e = 1.7$ keV. The last closed-flux surface in TEXTOR is determined by the toroidal limiter ALT-II, r = 46 cm.

As shown in Fig. 4, the W^{30+} density profiles are wide for the low-density/high-temperature case with a maximum at $r = 15$ cm, while the high-density/low-temperature case shows peaked W^{30+} density profiles for flat W concentration profiles. As for peaked W concentration profiles, the W^{30+} density profiles are always peaked, because in these cases the electron densities are always higher and the electron temperature lower that W does not get ionized beyond 30+ significantly. The W^{30+} density profiles were used to calculate line-integrals to be able to compare them to the XUV spectrometer data. As a result, the error in cross-calibration can be as high as 150% for the low-density case and 20% for the high-density case. Since the calibration to bolometry was done at low densities, the error of the absolute W-density could be as large as 150%. However, the relative error in the W-density for discharges at high density in RI mode (as will be discussed below) for the various auxiliary heating schemes is less than 20%. The tungsten concentrations obtained with the XUV spectrometer in this way can be as low as 1×10^{-5} (detection limit). The electron temperature at high densities was measured by an 11-channel ECE-diagnostic, using the third-harmonic ECE radiation.[32] The electron density profiles are provided by a nine-channel HCN interferometer.[33]

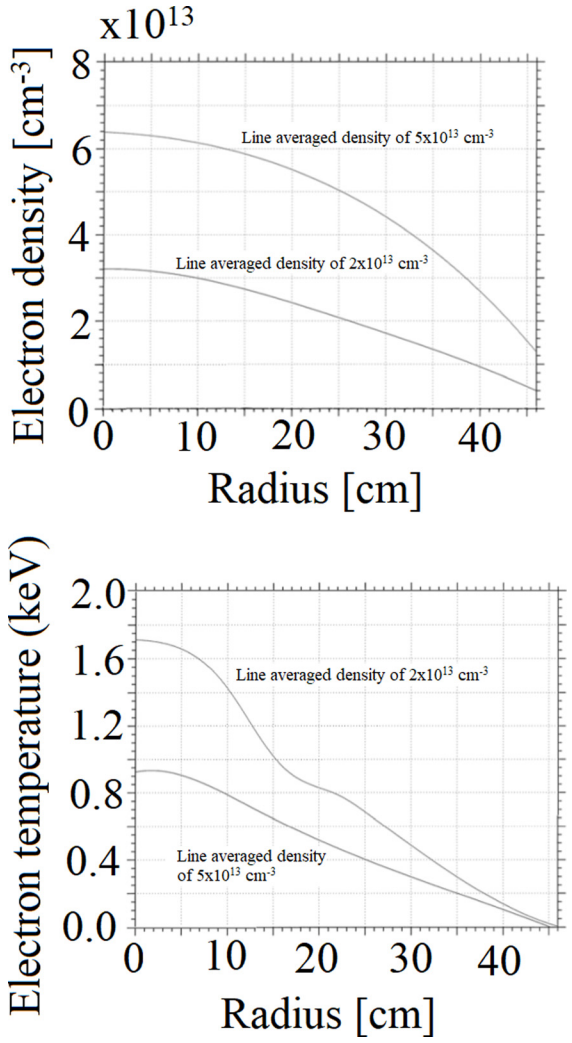

FIG. 5. Electron density and electron temperature profiles used for MIST simulations for two line-averaged densities $n_e = 5 \times 10^{13}$ cm^{-3}, and $n_e = 2 \times 10^{13}$ cm^{-3}. The last closed-flux surface in TEXTOR is determined by the toroidal limiter ALT-II, r = 0.46 m.

III. GENERAL CHARACTERIZATION OF TUNGSTEN SOURCES AND CORE CONCENTRATION IN IMPURITY SEEDED DISCHARGES

The experiments were performed mostly in RI-mode[14] operation (using neon seeding) with boronized walls. The neon radiation and thus the radiative power were kept constant during the discharge by feedback control of the NeVIII line emission throughout the discharge. Improved confinement in the RI mode occurs already at relatively low radiative power fractions of about 42%, as can be seen Fig. 7 by the increase in f_{H93} confinement enhancement factor. The confinement increases further toward $f_{H93} = 1$, when the radiative power fraction is further increased to higher levels (~73%).

To study the general behavior of the tungsten source and the tungsten density in the core, we varied the radial position of the test limiter, the total heating power, and the radiated power fraction. In a RI-mode plasma ($P_{heat} = 2.95$ MW, $n_e = 5.0 \times 10^{13}$ cm^{-3}, $I_p = 350$ kA), the position of the test limiter (r_L) was varied from 48 cm (withdrawn) to 45 cm (1 cm inside the last closed magnetic flux surface). The W-density in the plasma center increases up to 1.34×10^9 cm^{-3} for $r_L = 45$ cm, but no influence on the energy confinement was seen (Fig. 6). The confinement enhancement factor f_{H93}[34] was at a constant level of 0.91, which is almost as high as ELM-free H-mode scaling. Similar results were obtained on DIII-D.[35]

The impact of the seeded neon on the W-release and its influence on the plasma core is shown in Fig. 7, where the W-flux, the W-density, and the confinement enhancement factor f_{H93} are plotted vs the radiated power fraction γ_{rad} for a set of discharges, where in each discharge, the radiative power fraction was kept constant with successively increased radiative power fractions from discharge to discharge starting at 33 up to 73%. The edge density n_e (45 cm) remains constant, whereas T_e (45 cm) drops from 87 to 55 eV at the highest γ_{rad}. With increasing radiative power fraction (γ_{rad}), the f_{H93} rises and above γ_{rad} of approximately 42% the confinement is as good as ELMy

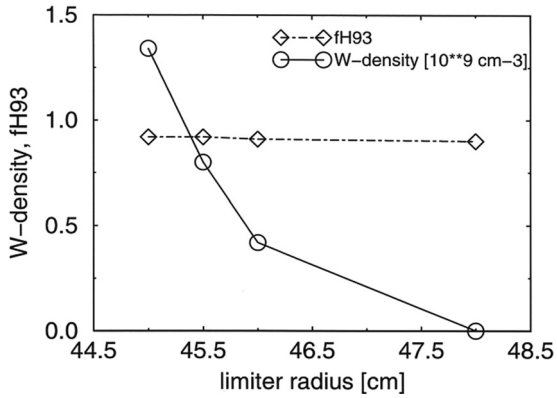

FIG. 6. Scan of tungsten test limiter position: W-density (10^9 cm^{-3}) in the plasma core and confinement enhancement factor f_{H93}. The last closed-flux surface as determined by the toroidal limiter ALT-II is at r = 46 cm.

H-mode. After a small increase, the W-flux is monotonically decreasing.

The small increase is due to the addition of neon, which enhances the W-source first before cooling of the plasma edge leads to lower impurity fluxes from carbon and oxygen and reduced sheath voltage drops. This shows up also in a decrease in the central W-density.

W-source calculations were performed like described in Ref. 36 and confirmed by ERO simulations by taking the measured values of the deuterium, carbon, oxygen, and neon fluxes.[25] The deuterium fluxes were obtained from D_α measurements. For the carbon fluxes, the line emission of CV was used, normalized to the deuterium fluxes. CV was chosen since the main carbon source in TEXTOR is the toroidal ALT-II limiter and carbon transported to the tungsten test limiter is then already charged to C^{4+}.[37] Hence, for the calculation of the W erosion by carbon, the main charge state of C^{4+} is used in determining the energy of the impinging impurity.

Assuming $T_e = T_i$, the energy of the impinging C^{4+} is then: $E = T_e(3Z + 2) = 14T_e$. The same approach was done for oxygen (O^{5+}) and neon (Ne^{2+}). The reason why for neon only the charge state of 2+ was chosen is because neon highly recycles on the tungsten limiter surface, and thus, lower charge states contribute more to the erosion.

In Fig. 8, the fractions of the sputtered W-flux caused by the different impinging species are displayed. The sum of all those different contributions results in the total W-flux, which is qualitatively in good agreement with the observed behavior of the W-influx with increasing radiation level shown in Fig. 7. The physical sputtering yields for electron temperatures between 55 and 87 eV for the impact of multiple-charged C^{4+} and O^{5+} on W changes by about 30% as Fig. 9 shows. This cannot fully explain the reduction in W-fluxes by about 64%. For comparison, the sputtering yield for Ne^{7+} is about 50% larger than that from Ne^{2+} (Fig. 9). Perhaps at lower radiative fraction, Ne^{7+} dominates and at higher radiative power fractions Ne^{2+}. This could potentially explain the behavior for $\gamma_{rad} > 0.6$. It will not change the conclusions though. Thus, the reduced W-flux is to a large extend a result of the reduction of the carbon and oxygen fluxes onto the W limiter, which occurs under RI-mode conditions. The contribution of the deuterium sputtering to the total erosion is negligible, and the W-flux released by neon is only slightly increased. The reduction of the carbon and oxygen fluxes under RI-mode conditions is a result of the reduced deuterium fluxes in this high-confinement regime and hence reduced carbon and oxygen sources from the main limiter ALT-II. The particle (deuteron) confinement is increased in the RI-mode leading to reduced deuteron fluxes at the edge, while maintaining high core densities.

On the first glance, this enhanced confinement in the plasma core, due to suppression of ITG-driven turbulence,[17] could be seen as a problem for the confinement of high-Z impurities.

However, as already stressed previously,[7] the tungsten core transport is mainly driven by neoclassical transport in TEXTOR. Figure 10 shows the energy confinement time in TEXTOR for discharges with neon (in RI mode) and without neon (L mode). A clear increase in energy confinement is seen for the neon seeded discharges with

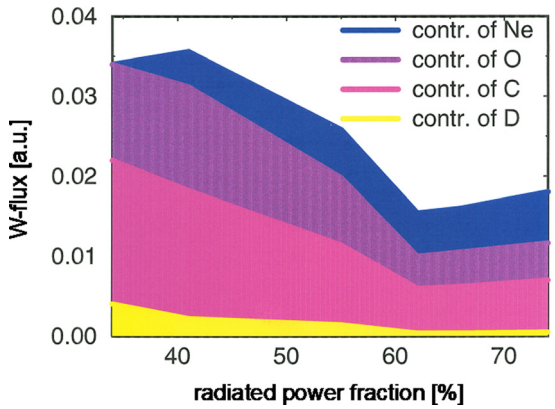

FIG. 8. Tungsten sputtering calculated as function of the radiated power fraction in neon seeded discharges in RI mode using sputter data of the Bohdansky[36] formula with measured fluxes of D, C^{4+}, O^{5+}, and Ne^{2+}.

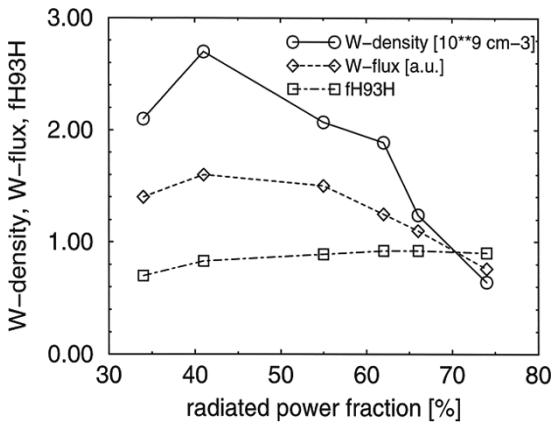

FIG. 7. W-density, W-flux, and confinement enhancement factor f_{H93} as function of the radiated power fraction in neon seeded discharges in RI-mode, NBI: 0.85 MW, ICRH: 1.85 MW, $I_p = 350$ kA, line-averaged $n_e = 5.0 \times 10^{13}$ cm^{-3}, r(limiter) = 45 cm.

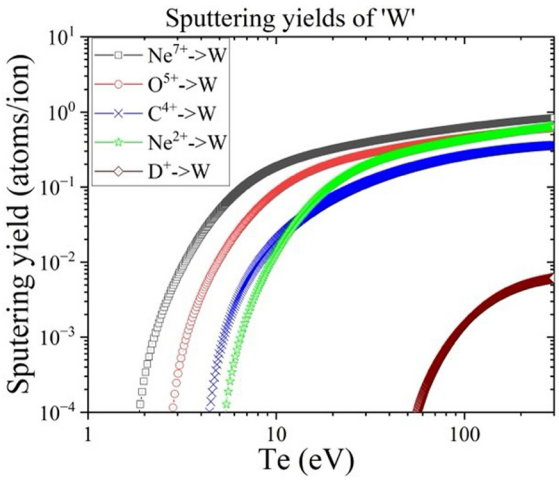

FIG. 9. Tungsten sputtering yield calculated as function of T_e assuming $T_e = T_i$ for C^{4+}, O^{5+}, Ne^{2+}, Ne^{7+}, and D using the Bohdansky[36] formula.

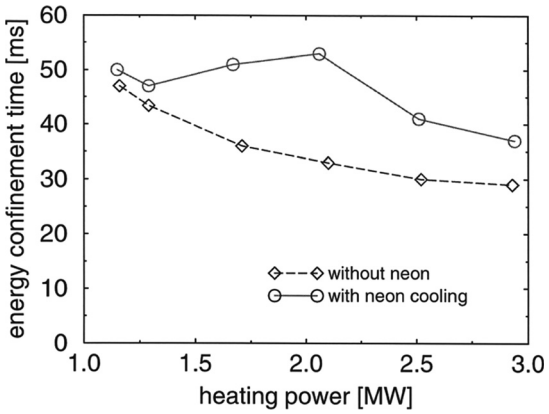

FIG. 10. Energy confinement time in TEXTOR as function of heating power for discharges with neon seeding (RI mode) and without neon seeding.

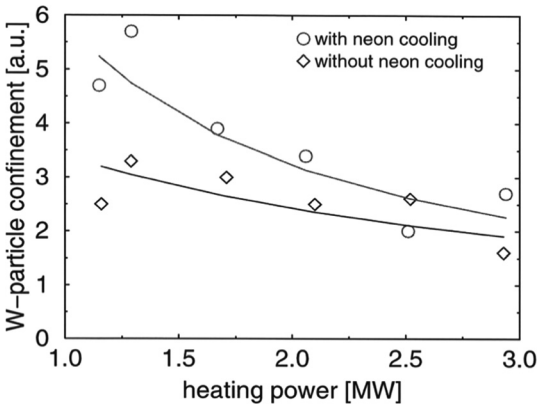

FIG. 11. Tungsten-particle confinement time as function of heating power for discharges with neon seeding (RI mode) and without neon seeding.

medium heating power. Figure 11 shows the tungsten-particle confinement time vs heating power for neon seeded discharges and discharges without neon seeding. Generally, an increase in tungsten confinement is seen with neon seeding. However, the pronounced increase in confinement at 2 MW in the energy confinement is not reflected in the tungsten confinement. This hints to different physics at play for the global energy confinement and the tungsten particle confinement. In the following, the effect of the heating on the tungsten release and transport is investigated in more detail.

IV. DIFFERENCE IN HEATING SCHEMES

In the investigations below, the plasma was heated with deuterium NBI alone or with deuterium NBI in combination with ICRH (H-minority heating). For the direct comparison of ICRF and NBI heating, two discharge series are presented. In the first discharge series, NBI and ICRF heating were compared for RI-mode operation, in which γ_{rad} was varied by the amount of neon seeding (line-averaged n_e $\sim 5.0 \times 10^{13}$ cm^{-3}, $I_p = 420$ kA, test limiter position 46 cm): (1) dominated by NBI heating ($P_{NBI} = 1.6$ MW, $P_{ICRF} = 0.5$ MW); (2) dominated by ICRF heating ($P_{NBI} = 0.5$ MW, $P_{ICRF} = 1.3$ MW). The central electron temperature in those discharges was between 1.4 and 1.5 keV, which means that the W-quasicontinuum is mostly radiating from the plasma core: $r < 0.3a_{min}$. Figure 12 shows the absolute neutral fluxes of tungsten at the test limiter. The net-influx of tungsten is about a factor of 2 lower due to the prompt redeposition of tungsten. From Fig. 12, one could get the impression that in the NBI-dominated discharges, the W-source is almost independent of γ_{rad}. However, the reason that no data are shown at higher γ_{rad} for the NBI-dominated discharges is because tungsten accumulation instabilities develop for $\gamma_{rad} = 73\%$. In the case of ICRF heating, the W-source decreases somewhat with increasing γ_{rad}. This is mainly due to the reduced fluxes of D, C and O at the limiter surface and only partly due to a reduced electron temperature at the edge as discussed above. Yet quantitatively, the W-source is not much different in both heating scenarios. The fact that the W-source is slightly lower in ICRF-heated discharges at radiated power fractions of 50% is due to the fact that the total heating power is about 5% lower in the ICRF-heated discharges when compared to the NBI-heated discharges. T_e (46 cm) is reduced from 75 eV (NBI-heated case) to 73 eV (ICRF-heated case), while n_e (46 cm) remains at 6×10^{12} cm^{-3}.

The tungsten densities behave similar to the W-source, as can be seen in Fig. 13. Accumulation of tungsten occurred just for $\gamma_{rad} = 73\%$ in the NBI-heated case. In predominantly ICRF-heated plasmas, no accumulation was observed, which is in agreement with previous results.[38] In the NBI-dominated discharges, the neon cooling leads to a strong peaking of the density profile (see Fig. 15) and an enhancement factor for the energy confinement time $f_{H93} = 1.03$ for γ_{rad} values larger than approximately 70%. In the ICRF-dominated case, the electron density profile steepens only a little bit and f_{H93} saturates at 0.85. The higher confinement in the NBI-dominated case results in edge electron temperatures, which are higher (80 eV at $\gamma_{rad} = 0.37$ and 71 eV at $\gamma_{rad} = 0.73$), when compared to the ICRF-dominated discharges (75 eV at $f_{rad} = 0.36$ and 59 eV at $f_{rad} = 0.75$).

Since the development of an accumulation instability depends on the strength of the source and the transport properties, the neoclassical convective velocity v_{neo} of the tungsten ions was calculated for both heating schemes (see Fig. 14). The solid lines show v_{neo} for the

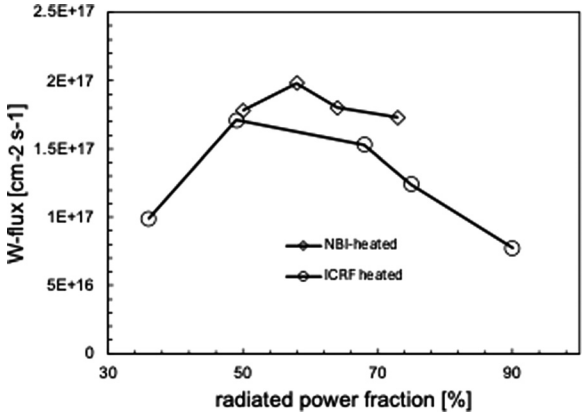

FIG. 12. Tungsten neutral flux as function of radiated power fraction in neon seeded discharges (RI mode) for different heating scenarios (NBI-dominated and ICRH-dominated).

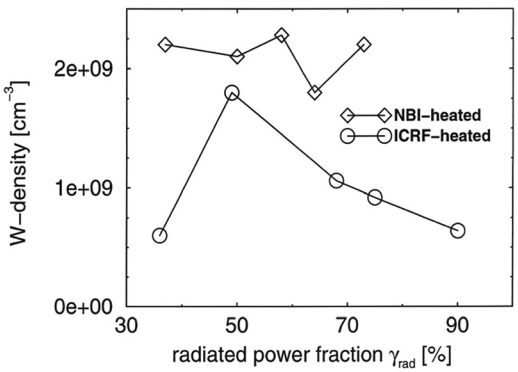

FIG. 13. Tungsten density in the plasma core as function of radiated power fraction in neon seeded discharges (RI-mode) for different heating scenarios (NBI-dominated and ICRH-dominated).

simplified case, considering the friction between tungsten and the deuterons only. The dashed lines in Fig. 14 display v_{neo} including impurity–impurity friction by using approximated profiles for carbon, oxygen and neon provided by the self-consistent radiation impurity transport model (RITM).[38]

For the discharges modeled here, the central concentrations of the impurities are as follows: 0.5% C; 0.1% O; and 1% Ne at the high radiative power fractions. A more detailed study on the influence of neon on the neoclassical transport properties can be found in Ref. 7. A direct comparison for the two heating scenarios (γ_{rad} approximately 75%) shows that over a large region of the plasma minor radius (5–25 cm), v_{neo} is directed outward (approximately 80 cm/s) for ICRF heating, whereas for NBI heating, it is directed inward (~20 cm/s). This is mainly a result of the strong electron density peaking in the case of predominant NBI heating.

In Figs. 15 and 16, the electron density peaking and electron temperature profiles are shown for the NBI-dominated heated discharges, when compared with ICRF-dominated discharges. However, additionally, the temperature profile is broader in the case of NBI heating, enhancing the neoclassical inward drift. Note that the 50 kV NBI injection has a broader power deposition profile than the ICRF heating. Since the energy confinement is higher with NBI than with ICRF heating, it seems to suggest that the increased W-source together with the increased global energy confinement is responsible for the accumulation. Therefore, a second series of discharges was performed to investigate a possible influence of the energy confinement on the tungsten particle confinement.

The radiated power fraction was kept constant $\gamma_{rad} \sim 65\%$, and ICRH was compared with NBI heating by applying the energy feedback system.[39] With increasing NBI power, the energy content of the plasma was feedback-controlled and kept constant ($E_{dia} = 130$ kJ) by acting on the level of ICRH power. Figure 17 shows the difference in the electron temperature and electron density profiles.

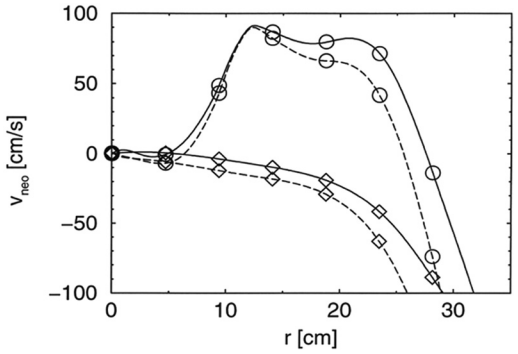

FIG. 14. Neoclassical convective velocity for ICRF-dominated (circles) and NBI-dominated (diamonds) heated discharge conditions; solid lines: considering collisions between tungsten and deuterons only, dashed lines: including collisions between tungsten and light impurities (1% neon). This was calculated for radiative power fraction of about 74%.

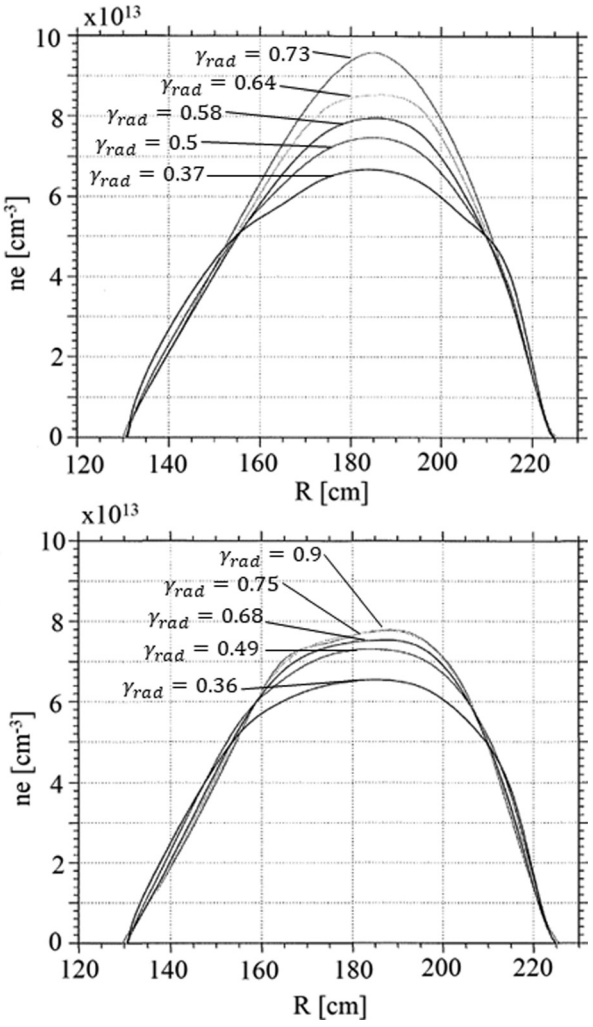

FIG. 15. Electron density profiles for γ_{rad}-scan with neon seeding; top figure: NBI-dominated heated discharges, from low central n_e to high central n_e: $\gamma_{rad} = 0.37$ (#71 609, no neon), $\gamma_{rad} = 0.5$ (#71 605), $\gamma_{rad} = 0.58$ (#71 606), $\gamma_{rad} = 0.64$ (#71 608), $\gamma_{rad} = 0.73$ (#71 610); bottom figure: ICRF-dominated heated discharges, from low central n_e to high central n_e: $\gamma_{rad} = 0.36$ (#71 615, no neon), $\gamma_{rad} = 0.49$ (#71 616), $\gamma_{rad} = 0.68$ (#71 617), $\gamma_{rad} = 0.75$ (#71 618), $\gamma_{rad} = 0.9$ (#71 619).

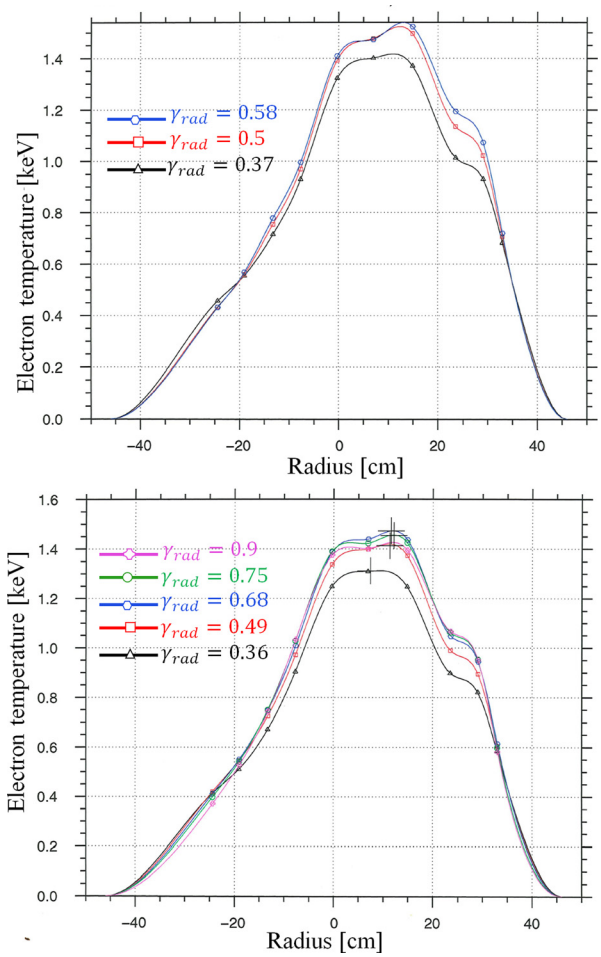

FIG. 16. Electron temperature profiles for γ_{rad}-scan with neon seeding; top figure: NBI-dominated heated discharges: $\gamma_{rad} = 0.37$ (#71 609, no neon, black), $\gamma_{rad} = 0.5$ (#71 605, red), $\gamma_{rad} = 0.58$ (#71 606, blue); bottom figure: ICRF-dominated heated discharges: $\gamma_{rad} = 0.36$ (#71 615, no neon, black), $\gamma_{rad} = 0.49$ (#71 616, red), $\gamma_{rad} = 0.68$ (#71 617, blue), $\gamma_{rad} = 0.75$ (#71 618, green), $\gamma_{rad} = 0.9$ (#71 619, purple).

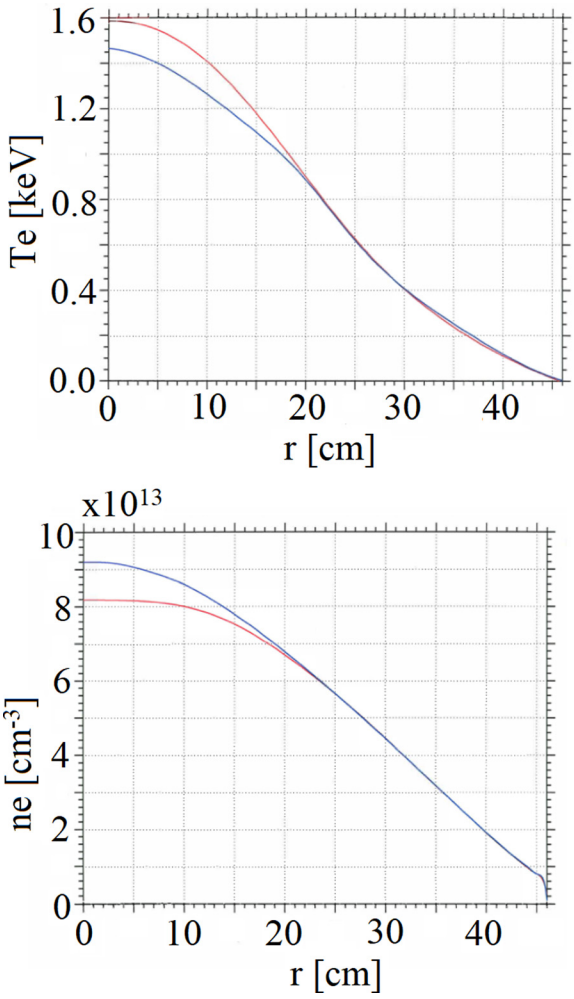

FIG. 17. Flux-surface averaged radial electron temperature and electron density profiles for $P_{NBI}/P_{ICRF} = 1$ (red lines, #71 626) and $P_{NBI}/P_{ICRF} = 2.5$ (blue lines, #71 628).

The impact of the ICRF vs the NBI heating scheme is mainly restricted on the plasma within a radius of about 23 cm in the plasma core. The ratio between the ICRF and NBI power, which was varied from shot to shot, is shown in Fig. 18. In the discharges #71 624 and #71 625, the preset energy was not reached. For the discharges #71 626–#71 628, an f_{H93} of ~0.9 was reached. In those discharges, no significant difference in the W-source was found. In all cases, the tungsten influx was about: $\Gamma_W = 8.3 \times 10^{16}\,cm^{-2}s^{-1}$. T_e is about 10% higher in #71 628 when compared to #71 626. However, the prompt redeposition would increase at that higher T_e, since ionization–mean free path is reduced. Nevertheless, accumulation of tungsten did occur in the case of $P_{NBI}/P_{ICRF} = 2.5$. Again, a comparison of the neoclassical convective velocity demonstrates the importance of the neoclassical transport on the development of the accumulation instability, as shown in Fig. 19. It should be mentioned here that an influence of the discharge history, i.e., a stronger W-release in the start phase of the discharge, on the later development of the central tungsten density cannot be ruled out. In pure D → D NBI-operated discharges (n_e approximately $5.0 \times 10^{13}\,cm^{-3}$, $I_p = 350$ kA, test limiter position 45.5 cm), a threshold for W-accumulation was observed, when the γ_{rad} exceeded 65% (see Fig. 20).

V. DISCUSSION

In this work, the release of tungsten from a tungsten test limiter was characterized for neon seeded discharge in RI modes. The neutral tungsten influx was determined absolutely. The ion influx is significantly lower due to prompt redeposition. The W-influx is reduced at higher radiative power fractions mainly due to reduced physical sputtering by carbon and oxygen, while neon does not add significantly to the erosion of tungsten at higher radiative power fractions.

It was found that the neoclassical transport of tungsten is influenced by collisions with light impurities (neon). The ratio between ICRF and NBI power in RI-mode discharges can largely influence the

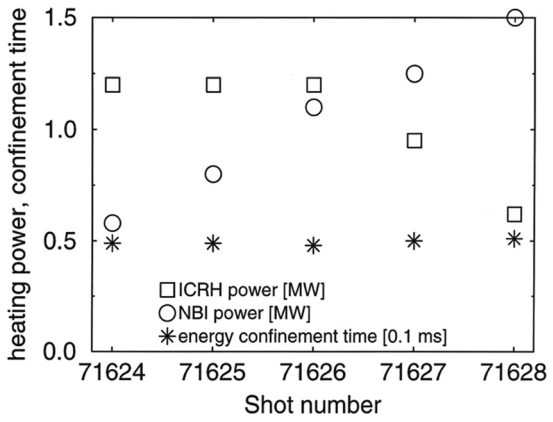

FIG. 18. ICRF power, NBI power, and the energy confinement time τ_e.

profiles of the electron temperature and density. This changes the neoclassical transport properties of high-Z elements like tungsten significantly. For predominantly NBI-heated discharges, the electron density profiles are steep, while for predominately ICRF-heated plasmas, the electron density profiles in the center of the plasma are flat. In TEXTOR, the neoclassical transport of tungsten is very collisional for all operation regimes independent of the heating scheme used and is in the so-called Pfirsch–Schlüter regime.

Hence, in these predominately ICRF-heated discharges, the neoclassical convective velocity is directed outward leading to temperature screening of tungsten over a large part of the plasma radius ($r/a < 0.6$). In the predominantly NBI-heated discharges, electron density profile is steep and the neoclassical convective velocity is directed inward over the whole plasma radius.

Previously, it was found that the tungsten transport in the core of TEXTOR is neoclassical in the absence of sawteeth.[7] In the discharges discussed here, sawteeth are present which add to the diffusion of tungsten in the core.[7]

The main question arises, if anomalous transport and changes of it can have a significant effect on the tungsten transport in the plasma core. Some theories predict that local heating by ICRF or electron cyclotron resonance heating (ECRH) can increase the anomalous particle transport[40] and that this also applies to the tungsten transport.

Self-consistent gyrokinetic modeling of neoclassical and turbulent impurity transport showed that both collisional (neoclassical) and turbulent transport contribute to the impurity flux.[41] The important question then is related to the relative magnitudes of the impurity transport channel and the nature of the turbulent transport. Is the turbulent transport TEM-driven or ITG-driven? While neon contributes to the neoclassical transport and enhances the tungsten confinement time in the plasma, the RI-mode confinement enhancement due to ITG-turbulence suppression does not have an effect on the tungsten confinement time as it has on the global confinement time. This is also demonstrated in a set of discharges where the heating mix and hence the neoclassical transport were changed without influence on the global energy confinement. In predominately NBI-heated discharges, the electron density is more peaked, likely due to beam fueling,[18] while predominately ICRF-heated discharges have flat density profiles in the plasma center in the absence of core fueling. Tungsten accumulation was only found in predominately NBI-heated discharges. This is consistent with previous work, where it was clearly demonstrated that the tungsten core density increases for radiative power fractions larger than 65%.[7] In RI-mode discharges in general and reported here, ITG turbulence is suppressed by injection of neon in the highly collisional plasmas.[17,18] For NBI-dominated heated discharges, this ITG-turbulence suppression is over most of the plasma radius. In the center ($0.05\,\mathrm{m} < r < 0.10\,\mathrm{m}$), the $\eta_i = (1/T_e\, dT_e/dr)/(1/n_e dn_e/dr)$ is about 2 in the NBI-dominant heated discharges and hence is marginal unstable for ITG modes but likely in balance with dissipative TEM. An η_i of about 1.5 is thought to be the threshold for ITG-turbulence growth. In ICRF-dominant heated discharges, the center of the plasma ($r < 0.25\,\mathrm{cm}$) shows flatter n_e profiles, due to the absence of fueling from NBI, and the η_i is about 8. This could potentially allow for some ITG-driven turbulence, although no significant difference in electron

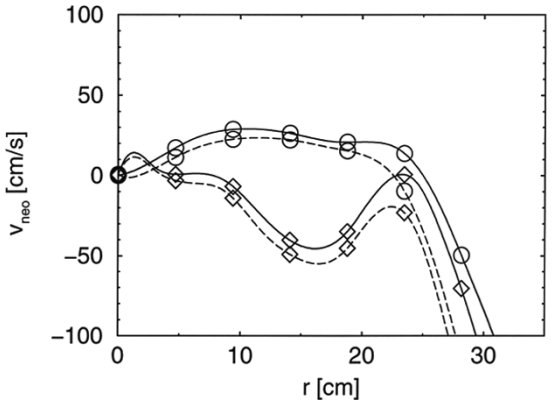

FIG. 19. Neoclassical convective velocity for $P_{NBI}/P_{ICRF} = 1$ (circles) and $P_{NBI}/P_{ICRF} = 2.5$ (diamonds); solid lines: considering collisions between tungsten and deuterons only, dashed lines: including collisions between tungsten and light impurities (1% neon).

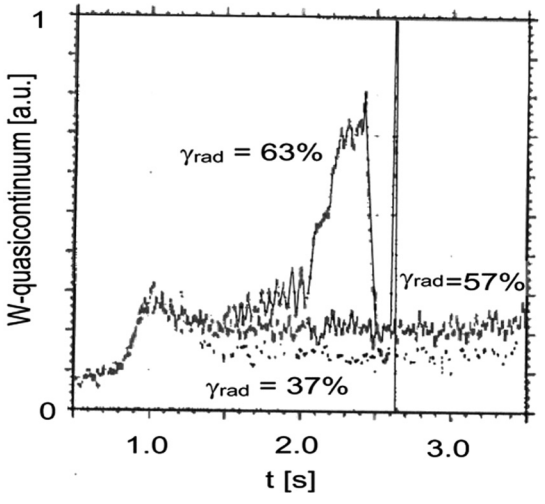

FIG. 20. W-quasicontinuum line emission for three different radiative power fractions for pure D → D NBI-operated discharges.

temperature profiles was observed. However, one should note that this only affects the very plasma core where $q < 1$ and sawteeth activity will dominate the transport. For NBI-dominant heated discharges, the neoclassical transport definitely dominates and leads to the tungsten accumulation.

Investigations on HL-2A showed that tungsten injection reduces turbulence levels by itself.[42] Thus, it is believed that in the RI-mode discharges, turbulent transport is less significant in the tungsten transport. This is also corroborated by the heating power scan, where the global energy confinement does not change (Fig. 18), but the tungsten transport does change significantly.

In addition, the change between ICRF and NBI changes the torque into the plasma, which can change the neoclassical transport of tungsten. More torque will lead to poloidal asymmetries in the tungsten distribution and hence increase the convective velocity of tungsten into the core.[43–45] This could play a role in the observations made here on TEXTOR.

Furthermore, as already indicated above, fueling by NBI in the plasma core will have a significant effect on the density profile and hence the neoclassical transport. This effect was previously studied for JET.[44] With predominately ICRF-heated plasmas, this particle source is strongly reduced and leads to flat electron density profiles in the core plasma in TEXTOR.

ICRF can influence the sawtooth behavior though. Frequent sawteeth are one way to keep the tungsten concentration low in the plasma core.[44]

Parametric dependence of the experimental tungsten transport coefficients in ICRH and ECRH plasmas in AUG H-modes showed a similar behavior as in TEXTOR.[46] The diffusion coefficient remains unchanged at the neoclassical level when ICRH or ECRH is applied; however, the neoclassical pinch velocity changes. This is the main driver for reducing impurity accumulation in the center of the plasma.

The results presented here might be of interest for ITER startup scenarios. ICRH and presumably ECRH could be used for early heating scenarios to avoid tungsten accumulation in the plasma center. Additionally, neon seeding could potentially reduce the tungsten sources by reducing the physical sputtering by intrinsic light impurities. Early RI mode could be considered to reduce the fluxes to the wall. The results from TEXTOR show similar conditions in ITER ($T_{e,LCFS}$, $n_{e,LCFS}$, P_{SOL}) that using neon seeding and central heating can avoid impurity accumulation of tungsten in the plasma core.

One can also try to estimate what the central heating requirements in TEXTOR mean for ITER. For this, the plasma volume for ITER and for TEXTOR and the total net tungsten source for both devices have to be estimated. For the volume, the ITER circular limiter plasma is approximately by a factor of 67 larger than the TEXTOR plasma. The toroidal wetted area is about a factor 200 larger in ITER than in TEXTOR, if the toroidal wetted fraction in ITER is 100%. Realistically, due to the shaping of the tiles to accommodate shadowing of gaps, etc., a toroidal wetted fraction of 50% is likely closer to reality. Hence, the toroidal wetted area is likely about a factor of 100 larger in ITER than in TEXTOR. The poloidal wetted area depends on the flux expansion close to the tangent of the circular plasma with the wall, and hence, it depends on the plasma minor radius in the case of ITER, and in the TEXTOR test limiter case, it depends on the test limiter spherical radius (~100 mm). Furthermore, it depends on the heat flux decay length λ_q. According to the scaling of Eich *et al.*,[47] λ_q is inverse proportional to the plasma current. If we take an average current of 6 MA for the limiter current ramp-up phase in ITER and for TEXTOR a steady-state plasma current of 350 kA, we find that the flux expansion due to the larger plasma radius (in comparison with the small radius of the test limiter in TEXTOR) cancel out with the lower λ_q predicted for ITER. From those estimates, it would appear that the tungsten source area would be a factor of 100 larger in ITER, when compared to TEXTOR. For the net-erosion, the detailed geometry is important in addition to the plasma parameters. The shallower angle of incidence in ITER should increase the prompt redeposition fraction, when compared to TEXTOR. It is expected that the prompt redeposition in ITER will be likely in the range of 90% using the simple formula from Ref. 24. Taking this into account, these simple estimates would lead to the conclusion that the ratio between tungsten source and plasma volume would be comparable in ITER and TEXTOR. However, one cannot derive from this crude analysis that a heating power of 67 times the ICRF heating power at TEXTOR is required to ensure that tungsten does not accumulate. The plasma core density and temperature profiles are completely different in ITER, and a detailed transport analysis is required. The discussion here should just frame obtained results in the context of ITER. Previously, a local heating power density for avoiding impurity accumulation showed good agreement with experiments.[48] Perhaps a similar analysis could be done for ITER.

In regular L-mode limiter discharges, where anomalous transport is larger in comparison with the neoclassical tungsten transport, the threshold might be different. These results cannot be used for extrapolations to H-mode discharges, where the profiles in the pedestal will largely determine the tungsten transport. These results should also not be compared to ICRF-heated H-mode discharges, where the main tungsten source is in the divertor.[49] The conditions are completely different in this case.

VI. SUMMARY AND CONCLUSION

The release and transport of tungsten in TEXTOR radiatively cooled discharges was investigated. The tungsten source from a test limiter has been characterized quantitatively. Physical sputtering by the light impurities of C, O, and Ne has been identified as the main source of tungsten. Seeding of neon did reduce the edge electron temperature and the intrinsic impurity fluxes to the W limiter, thus effectively reducing the W-source at high radiative power fractions. The tungsten transport was characterized for NBI- and ICRF-heated plasmas. The transport was found to be neoclassical in nature and impurity accumulation could be explained by the absence of temperature screening in the predominately NBI-heated discharges. Anomalous transport is thought to be negligible in the TEXTOR collisionality regime and in particular in the enhanced confinement regime RI-mode. Neon seeding will lead to an enhanced tungsten confinement time due to the increased neoclassical inward fluxes as a result of the friction between neon and tungsten. Tungsten accumulation can be avoided in the center of the plasma, when the ratio between $P_{ICRF}/P_{tot} > 0.5$ even at the highest radiative power fractions. These results are related to TEXTOR conditions in RI-mode operation scenarios where anomalous transport for tungsten does not play a role.

ACKNOWLEDGMENTS

This work was supported by the DOE Office of Science, Office of Fusion Energy Science, under Contract No. DE-AC-5-00OR22725.

AUTHOR DECLARATIONS

Conflict of Interest

The authors have no conflicts to disclose.

Author Contributions

J. Rapp: Conceptualization (lead); Data curation (lead); Formal analysis (lead); Investigation (lead); Methodology (lead); Project administration (equal); Software (equal); Supervision (equal); Visualization (lead); Writing – original draft (lead). **S. Brezinsek:** Resources (equal); Validation (equal); Writing – review & editing (equal). **G. D. Dhamale:** Formal analysis (supporting); Validation (supporting); Visualization (equal); Writing – review & editing (equal). **H. R. Koslowski:** Data curation (equal); Investigation (equal); Resources (equal); Software (equal); Writing – review & editing (equal). **A. Krämer-Flecken:** Data curation (equal); Investigation (equal); Resources (equal). **J. Ongena:** Investigation (equal); Resources (equal); Writing – original draft (equal). **G. Sergienko:** Resources (equal); Writing – review & editing (equal).

DATA AVAILABILITY

The data that support the findings of this study are available within the article.

REFERENCES

[1]M. Greenwald, A. Bader, S. Baek, M. Bakhtiari, H. Barnard, W. Beck, W. Bergerson, I. Bespamyatnov, P. Bonoli, D. Brower, D. Brunner, W. Burke, J. Candy, M. Churchill, I. Cziegler, A. Diallo, A. Dominguez, B. Duval, E. Edlund, P. Ennever, D. Ernst, I. Faust, C. Fiore, T. Fredian, O. Garcia, C. Gao, J. Goetz, T. Golfinopoulos, R. Granetz, O. Grulke, Z. Hartwig, S. Horne, N. Howard, A. Hubbard, J. Hughes, I. Hutchinson, J. Irby, V. Izzo, C. Kessel, B. LaBombard, C. Lau, C. Li, Y. Lin, B. Lipschultz, A. Loarte, E. Marmar, A. Mazurenko, G. McCracken, R. McDermott, O. Meneghini, D. Mikkelsen, D. Mossessian, R. Mumgaard, J. Myra, E. Nelson-Melby, R. Ochoukov, G. Olynyk, R. Parker, S. Pitcher, Y. Podpaly, M. Porkolab, M. Reinke, J. Rice, W. Rowan, A. Schmidt, S. Scott, S. Shiraiwa, J. Sierchio, N. Smick, J. A. Snipes, P. Snyder, B. Sorbom, J. Stillerman, C. Sung, Y. Takase, V. Tang, J. Terry, D. Terry, C. Theiler, A. Tronchin-James, N. Tsujii, R. Vieira, J. Walk, G. Wallace, A. White, D. Whyte, J. Wilson, S. Wolfe, G. Wright, J. Wright, S. Wukitch, and S. Zweben, Phys. Plasmas **21**(11), 110501 (2014).
[2]M. L. Apicella, R. Bartiromo, L. Gabellieri, V. P. Ridolfini, L. Pieroni, R. Zagorski, G. Bracco, F. Crisanti, D. Frigione, G. Gatti, H. Kroegler, G. Maddaluno, and G. Mazzitelli, Plasma Phys. Controlled Fusion **39**(8), 1153–1167 (1997).
[3]S. Brezinsek and JET-EFDA contributors, J. Nucl. Mater. **463**, 11–21 (2015).
[4]R. Neu, V. Bobkov, R. Dux, J. Fuchs, O. Gruber, A. Herrmann, A. Kallenbach, H. Maier, M. Mayer, and T. Pütterich, Phys. Scr. **2009**(T138), 014038.
[5]A. Eksaeva, A. Kirschner, J. Romazanov, S. Brezinsek, C. Linsmeier, F. Maviglia, M. Siccinio, and S. Ciattaglia, Phys. Scr. **97**(1), 014001 (2022).
[6]M. Rubel, S. Brezinsek, J. Coenen, A. Huber, A. Kirschner, A. Kreter, P. Petersson, V. Philipps, A. Pospieszczyk, and B. Schweer, Matter Radiat. Extremes **2**(3), 87–104 (2017).
[7]J. Rapp, M. Tokar, L. Könen, H. Koslowski, G. Bertschinger, M. Brix, H. Claassen, R. Jaspers, A. Krämer-Flecken, and K. Ohya, Plasma Phys. Controlled Fusion **39**(10), 1615 (1997).
[8]D. Fajardo, C. Angioni, R. Dux, E. Fable, U. Plank, O. Samoylov, G. Tardini, and ASDEX Upgrade Team, Nucl. Fusion **64**(4), 046021 (2024).
[9]V. V. Bobkov, F. Braun, R. Dux, A. Herrmann, L. Giannone, A. Kallenbach, A. Krivska, H. W. Müller, R. Neu, and J.-M. Noterdaeme, Nucl. Fusion **50**(3), 035004 (2010).
[10]S. J. Wukitch, R. Boivin, P. Bonoli, J. Goetz, J. Irby, I. Hutchinson, Y. Lin, A. Parisot, M. Porkolab, and E. Marmar, Plasma Phys. Controlled Fusion **46**(9), 1479 (2004).
[11]P. Maget, P. Manas, R. Dumont, C. Angioni, J. Artaud, C. Bourdelle, F. Casson, L. Colas, P. Devynck, and D. Fajardo, Plasma Phys. Controlled Fusion **65**(12), 125009 (2023).
[12]W. Zhang, G.-H. Zhu, X.-J. Zhang, G.-Q. Zhong, L. Ai, Y.-Q. Chu, T.-S. Fan, H.-C. Fan, Y.-Y. Guo, and B.-L. Hao, Nucl. Fusion **63**(5), 056015 (2023).
[13]G. Urbanczyk, X. Zhang, L. Zhang, L. Colas, R. Dumont, W. Tierens, E. Lerche, D. Van Eester, S. Heuraux, and X. Yang, Nucl. Fusion **60**(12), 126003 (2020).
[14]A. Messiaen, J. Ongena, U. Samm, B. Unterberg, G. Van Wassenhove, F. Durodie, R. Jaspers, M. Tokaŕ, P. Vandenplas, and G. Van Oost, Phys. Rev. Lett. **77**(12), 2487 (1996).
[15]A. Messiaen, J. Ongena, U. Samm, M. Tokar, B. Unterberg, D. Boucher, K. Finken, E. Hintz, R. Koch, and G. Mank, Nucl. Fusion **36**(1), 39 (1996).
[16]A. Messiaen, H. Conrads, M. Gaigneaux, J. Ongena, R. Weynants, G. Bertschinger, J. Beuken, P. Cornelissen, T. Delvigne, and F. Durodie, Plasma Phys. Controlled Fusion **32**(11), 889 (1990).
[17]M. Tokar, J. Ongena, B. Unterberg, and R. Weynants, Phys. Rev. Lett. **84**(5), 895 (2000).
[18]B. Unterberg, U. Samm, M. Tokar', A. Messiaen, J. Ongena, and R. Jaspers, Fusion Sci. Technol. **47**(2), 187–201 (2005).
[19]M. Tokar, J. Rapp, G. Bertschinger, L. Konen, H. Koslowski, A. Kramer-Flacken, V. Philipps, U. Samm, and B. Unterberg, Nucl. Fusion **37**(12), 1691 (1997).
[20]R. Pitts, A. Loarte, T. Wauters, M. Dubrov, Y. Gribov, F. Köchl, A. Pshenov, Y. Zhang, J. Artola, and X. Bonnin, Nucl. Mater. Energy **42**, 101854 (2025).
[21]M. Wada, T. Ohgo, A. Pospieszczyk, A. Huber, G. Sergienko, T. Tanabe, W. Biel, K. Kondo, K. Ohya, and V. Philipps, J. Nucl. Mater. **290–293**, 768–772 (2001).
[22]S. Brezinsek, M. Laengner, J. Coenen, M. O'Mullane, A. Pospieszczyk, G. Sergienko, and U. Samm, Phys. Scr. **2017**(T170), 014052.
[23]B. Schweer, G. Mank, A. Pospieszczyk, B. Brosda, and B. Pohlmeyer, J. Nucl. Mater. **196–198**, 174–178 (1992).
[24]G. Van Rooij, J. Coenen, L. Aho-Mantila, S. Brezinsek, M. Clever, R. Dux, M. Groth, K. Krieger, S. Marsen, and G. Matthews, J. Nucl. Mater. **438**, S42–S47 (2013).
[25]V. Philipps, A. Pospieszczyk, A. Huber, A. Kirschner, J. Rapp, B. Schweer, P. Wienhold, G. Van Oost, G. Sergienko, and T. Tanabe, J. Nucl. Mater. **258–263**, 858–864 (1998).
[26]K. Ohya, J. Kawata, T. Tanabe, M. Wada, Y. Ueda, V. Philipps, B. Unterberg, A. Pospieszczyk, B. Schweer, and F. Weschenfelder, J. Nucl. Mater. **258–263**, 1055–1059 (1998).
[27]U. Kögler, F. Weschenfelder, J. Winter, H. Esser, V. Philipps, A. Pospieszczyk, B. Schweer, J. Von Seggern, and P. Wienhold, J. Nucl. Mater. **241–243**, 816–820 (1997).
[28]S. Brezinsek, D. Borodin, J. Coenen, D. Kondratjew, M. Laengner, A. Pospieszczyk, U. Samm, and TEXTOR Team, Phys. Scr. **2011**(T145), 014016.
[29]D. E. Post, R. Jensen, C. Tarter, W. Grasberger, and W. Lokke, At. Data Nucl. Data Tables **20**(5), 397–439 (1977).
[30]T. Ohgo, M. Wada, A. Pospieszczyk, W. Biel, K. Kondo, T. Tanabe, T. Hirai, V. Philipps, A. Huber, and G. Sergienko, J. Nucl. Mater. **307–311**, 149–153 (2002).
[31]R. A. Hulse, Nucl. Technol./Fusion **3**(2), 259–272 (1983).

[32]A. Krämer-Flecken, K. Finken, H. Larue, and V. Udintsev, paper presented at the EC-12: Proceedings of the 12th Joint Workshop on Electron Cyclotron Emission and Electron Cyclotron Heating: Aix-en-Provence, France, 13–16 May 2002.
[33]H. Koslowski and H. Soltwisch, Fusion Eng. Des. **34–35**, 143–150 (1997).
[34]K. Thomsen, D. Campbell, J. Cordey, O. Kardaun, F. Ryter, U. Stroth, A. Kus, J. DeBoo, D. Schissel, and Y. Miura, Nucl. Fusion **34**(1), 131 (1994).
[35]G. Jackson, M. Murakami, G. Staebler, M. Wade, A. Messiaen, J. Ongena, B. Unterberg, J. Boedo, T. Evans, and A. Hyatt, J. Nucl. Mater. **266–269**, 380–385 (1999).
[36]J. Bohdansky, Nucl. Instrum. Methods Phys. Res., Sect. B **2**(1–3), 587–591 (1984).
[37]G. Telesca, H. Claassen, A. Pospieszczyk, R. Koch, and D. Van Eester, Nucl. Fusion **34**(5), 625 (1994).
[38]G. Van Oost, A. Messiaen, V. Philipps, R. Koch, A. Kramer-Flacken, K. Ohya, J. Ongena, A. Pospieszczyk, J. Rapp, M. Rubel, U. Samm, N. Schoon, B. Schweer, T. Tanabe, G. Telesca, M. Tokar, Y. Ueda, B. Unterberg, G. Van Wassenhove, M. Wada, and J. Winter, paper presented at the Europhysics Conference Abstracts (Proceedings of the 22nd EPS Conference on Controlled Fusion and Plasma Physics, Bournemouth, 1995), edited by B. Keen, P. Stott, and J. Winter, 1995.
[39]A. M. Messiaen, J. Ongena, B. Unterberg, F. Durodié, U. Samm, P. E. Vandenplas, G. Van Oost, G. Van Wassenhove, M. Vervier, R. R. Weynants, G. Bertschinger, J. Boedo, G. Bonheure, P. Dumortier, K. H. Finken, G. Fuchs, D. Hillis, R. Jaspers, R. Koch, L. Könen, H. R. Koslowski, A. Krämer-Flecken, A. Lyssoivan, G. Mank, A. Pospieszczyk, J. Rapp, B. Schweer, J. Schwelberger, G. Telesca, R. Uhlemann, G. Waidmann, J. Winter, and G. H. Wolf, AIP Conf. Proc. **403**(1), 41–48 (1997).
[40]J. Stober, R. Dux, O. Gruber, L. Horton, P. Lang, R. Lorenzini, C. Maggi, F. Meo, R. Neu, and J.-M. Noterdaeme, Nucl. Fusion **43**(10), 1265 (2003).
[41]D. Esteve, Y. Sarazin, X. Garbet, V. Grandgirard, S. Breton, P. Donnel, Y. Asahi, C. Bourdelle, G. Dif-Pradalier, and C. Ehrlacher, Nucl. Fusion **58**(3), 036013 (2018).
[42]Q. Zou, J. Cheng, Z. Shi, Y. Xu, L. Yan, C. Dong, X. Chen, W. Zhang, Y. Zhu, and Z. Huang, Nucl. Fusion **63**(12), 126029 (2023).
[43]C. Angioni, M. Sertoli, R. Bilato, V. Bobkov, A. Loarte, R. Ochoukov, T. Odstrcil, T. Pütterich, J. Stober, and ASDEX Upgrade Team, Nucl. Fusion **57**(5), 056015 (2017).
[44]S. Breton, F. Casson, C. Bourdelle, J. Citrin, Y. Baranov, Y. Camenen, C. Challis, G. Corrigan, J. Garcia, and L. Garzotti, Nucl. Fusion **58**(9), 096003 (2018).
[45]F. Casson, H. Patten, C. Bourdelle, S. Breton, J. Citrin, F. Koechl, M. Sertoli, C. Angioni, Y. Baranov, and R. Bilato, Nucl. Fusion **60**(6), 066029 (2020).
[46]M. Sertoli, C. Angioni, T. Odstrcil, ASDEX Upgrade Team, and EUROFusion MST1 Team, Phys. Plasmas **24**(11), 112503 (2017).
[47]T. Eich, A. Leonard, R. Pitts, W. Fundamenski, R. J. Goldston, T. Gray, A. Herrmann, A. Kirk, A. Kallenbach, and O. Kardaun, Nucl. Fusion **53**(9), 093031 (2013).
[48]M. Nave, J. Rapp, T. Bolzonella, R. Dux, M. Mantsinen, R. Budny, P. Dumortier, M. Von Hellermann, S. Jachmich, and H. Koslowski, Nucl. Fusion **43**(10), 1204 (2003).
[49]E. Lerche, M. Goniche, P. Jacquet, D. Van Eester, V. Bobkov, L. Colas, C. Giroud, I. Monakhov, F. Casson, and F. Rimini, Nucl. Fusion **56**(3), 036022 (2016).